

Real-time process monitoring and closed-loop control on laser power via a customized laser powder bed fusion platform

Rongxuan Wang¹, Benjamin Standfield¹, Chaoran Dou¹, Andrew C. Law², Zhenyu James Kong^{*,1}

Grado Department of Industrial and Systems Engineering, Virginia Tech, Blacksburg, VA 24060, USA



ARTICLE INFO

Keywords:
 Laser powder bed fusion
 Process monitoring
 Closed-loop control
 3D scanning
 Quality control

ABSTRACT

Additive manufacturing (AM) is one of the most effective ways to fabricate parts with complex geometries using various materials. However, AM also suffers from printing quality issues resulting from the defects such as over-melt, lack of fusion, swelling, etc. One of the root causes of those issues is that the process parameters remain constant during the entire printing process, regardless of the dynamic heat accumulation and various printing feature sizes. For instance, raster is the most common scanning strategy in the laser powder bed fusion (L-PBF) process. The length of the raster line varies depending on the printing feature size. When scanning small features, the raster line is short, resulting in heat accumulations and over-melt. These variabilities may cause severe quality issues and thus suggest adaptive process parameters be applied. Aiming to address this challenge, this study develops a closed-loop control system to regulate the laser power based on melt pool thermal emission to avoid over-melt, balling, and high surface roughness. The control target is determined by correlating the printing quality (dimensional printing error in this study) with the thermal emission through thin-line printing trials using variable power. A high-speed thermal sensor and controller are designed, tuned, and implemented on a newly developed L-PBF testbed. The system successfully maintains a low dimensional error by regulating the laser power at 2 kHz. A significant improvement in printing quality was achieved, as validated by both microscopic imaging and 3D scanning.

1. Introduction

1.1. Background

The popularity of additive manufacturing (AM) has increased dramatically in the past decade, given the advantage that it can effectively fabricate parts with complex geometry. Among the AM processes, laser powder bed fusion (L-PBF) has been intensively studied because it is ideal for metal 3D printing. L-PBF forms the part geometry using a high energy density laser beam to selectively melt metal powder onto the substrate [1–4]. This technology has been widely used in many industries, such as aviation, medical, and military [5,6]. However, hindered by a large number of process parameters and non-steady-state printing, high-quality printing is still hard to achieve. Specifically, the

L-PBF process parameters include hatch spacing, hatch pattern, hatch angle, layer height, powder size, laser spot size, laser power, laser speed, delay time, protection gas flow rate, etc. In addition, the non-steady state of the printing can be caused by the variation of powder packing, re-melting, heat accumulation, spatters, un-uniform powder spreading, and others.

L-PBF fabricates parts lay by layer, and each layer is filled by melt tracks. Raster, a tool path generation strategy filling area by parallel lines, is the most common scanning pattern in L-PBF. However, using a fixed laser power regardless of raster length and printing feature size (thin wall or pointy regions less than 400 μm are commonly referred to as small features in L-PBF) will cause several quality issues [7]. Miniature features or sharp corners have short raster lines. In this scenario, heat will accumulate and cause over melt (see Fig. 1a). The root cause of

Abbreviations: L-PBF, Laser powder bed fusion; PID, Proportional-integral-derivative controller; FOV, Field of view; LDR, Light-dependent resistor (photoresistor); ROI, Resolution of interest; TEI, Thermal emission index (the reading of the proposed sensor).

* Corresponding author.

E-mail address: zkong@vt.edu (Z.J. Kong).

¹ Virginia Tech

² IoTEx

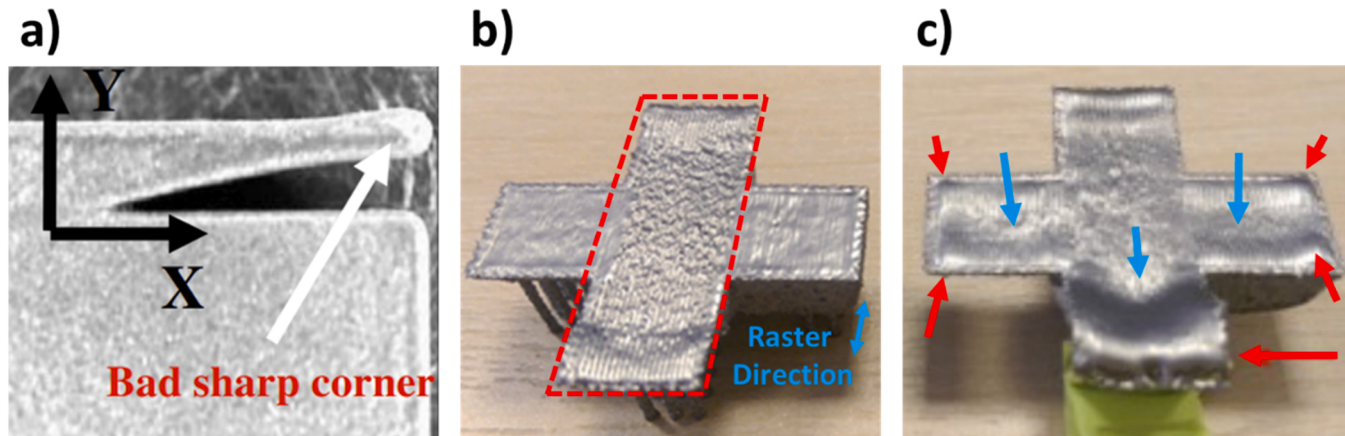


Fig. 1. a) An oversized sharp corner due to heat accumulation [8]. b) Example of insufficient melt and high surface roughness (red dash region) [9]. c) Dents and swellings due to excessive power, indicated by blue and red arrows, respectively [9].

the heat accumulation is the insufficient cooling time of the previous melt path when the laser melts the adjacent area again [8]. When this problem occurs, shape accuracy cannot be ensured. In addition, the over melt will cause microstructure inconsistency resulting from inconsistent cooling rates and thermal gradients. A severe porosity may occur since the melt pool has a strong keyhole. In contrast, large features have long raster lines and less heat accumulation. If the laser power is low, favoring small feature printing quality, an insufficient melt will occur on large features. Such phenomenon can cause defects such as high surface roughness, balling, and lack of fusion [9]. As Fig. 1b illustrates, the entire printing area is scanned by raster lines. The lines are short on two sides and long at the center. The laser power is set to ensure that the two side-square regions have a high surface printing quality. However, the center region (marked in the red dash) with long raster lines suffers from insufficient melt and poor surface roughness because the heat has been overly dissipated. Additionally, as Fig. 1c shows, swelling (humping) and denting will occur when the laser power stays high [9,10]. This phenomenon is due to the laser's evaporation pressure pushing the melted material to the back of the scan track, which could be solved by properly regulating the laser power [9]. Swelling and denting are especially severe when the laser speed is high ($> 800 \text{ mm/s}$), preventing the printing efficiency from being further improved [10]. Therefore, constant laser power is problematic, especially when the printed shape is relatively complex. All the above quality issues inspired this work to achieve consistent melting through real-time adaptive laser power control based on thermal sensing.

1.2. Related literature

In-process quality control includes feedforward and feedback controls [8,11]. Feedforward (open-loop control) is a strategy to ensure quality by assigning proper process parameters before printing based on offline modeling or simulation. In contrast, feedback control (closed-loop control) uses an in-situ sensing device and an algorithm to update the process parameters until the desired quality has been achieved. Feedback control is generally considered more effective and robust because complex processes, especially those with high variability, are challenging to model and predict. However, it is hard to achieve feedback control since it requires (1) establishing the processing signature to quality correlation, (2) sensing and transferring the processing signature in high-speed and real-time, (3) adjusting the process parameter efficiently, and (4) a platform to implement the control. This section firstly reviews the feedforward control works related to powder bed fusion, then analyzes the need, challenge, and current research progress in L-PBF feedback control.

Most current research uses a feedforward control strategy to improve

quality since the printing geometry and material thermal properties are known before printing. Yeung et al. proposed a jerk-limited path design strategy to solve the scanned shape inaccuracy due to galvanometer acceleration [12]. Following that, Yeung et al. implemented an algorithm to reduce the effect of heat accumulation by scaling down the laser power when an edge or overhanging structure is being printed [13]. Yeung et al. also designed several unique tool paths to improve printing consistency [14]. Researchers also tried to solve the heat accumulation problem by optimizing the scan strategy. For example, Dehoff et al. designed a sequential raster approach to melt the powder with spatially discretized squares and proved that different scan strategies could tailor the microstructure [15,16]. Shao et al. discovered the effect of ordered and random spot melt strategies compared with the traditional raster scan [17]. They found that spot scan strategies can yield more refined grain structures through thermal gradients and cooling rate tailoring. Ramani et al. developed a thermal modeling-based sequential raster strategy to reduce the effect of heat accumulation [18]. The complex scan strategy can reduce the local heat accumulation, but only to a certain extent. With the checkerboard strategy, heat accumulation still happens for each small square [19]. When sequential methods apply, the temperature will gradually build up by the end because the location options to scan without heat accumulation will eventually run out [15, 18]. Additionally, complex scan strategies also slow the printing process due to extra tool paths and laser delays.

Even though significant efforts have been devoted, due to the complex nature of L-PBF, developing an effective feedforward control model is challenging. For example, the droplet due to spattering and powder spreading quality are highly random, limiting the effectiveness of modeling-based feedforward control. Therefore, feedback control is necessary since it can adaptively compensate for the disturbances. Researchers have already established correlations between the process signatures and the printing quality metrics, enabling the feasibility of in-process control in L-PBF. For example, Clijsters et al. linked the co-axial camera data with the presentation of the porosities [20]. Liu et al. used deep learning to predict the print's surface roughness based on monochrome images [21]. Kruth et al. discovered that the photodiode signal proportionally correlates with the melt pool size [8]. Wang et al. found IR data, especially the total thermal emission, could be used to determine melt pool geometry and keyhole information [22]. However, the correlation between process signatures and dimensional accuracy has not been addressed yet.

Numerous challenges also exist in process signature sensing, parameter adjusting, and proper L-PBF machine that support the sensing and control, impeding the completion of the feedback control. Specifically, L-PBF is a very rapid process. The laser speed consistently exceeds a few hundred, even over a thousand millimeters per second, which

requires high-speed sensing and control capability ($> 1 \text{ kHz}$). Even though high-speed sensing has been developed for years, real-time data transfer and processing with a high speed are still challenging. Unlike the feedforward control, the processing parameters suitable to be adjusted in high-speed feedback control are limited.

To be specific, process parameters that directly contribute to the input volumetric energy density in L-PBF include hatch spacing, layer height, laser spot size, laser speed, and laser power [23]. They will all affect the melt pool size, melt pool shape, and cooling rates. However, not all of them are suitable for high-speed closed-loop control. Laser spot size generally is un-adjustable during printing. Layer height can only be changed after the current layer is finished. Scanning speed and hatch spacing modification require rewriting and re-uploading the entire printing program since the galvanometer motion needs to be synchronized with the laser firing timing. Altering the scanning speed and hatch spacing requires high computational power and data transfer speed, making it nearly impossible to achieve at high-speed (over 1 kHz) by current technologies. Laser power, on the other hand, is the only suitable parameter for high-speed real-time control because it can be controlled directly and independently. Moreover, feedback control requires in-process parameter adjustment. However, commercial L-PBF machines generally prohibit sensing installation and in-process machine adjustment.

Despite all these challenges, researchers have already attempted to implement feedback control in L-PBF. Vasileska et al. used a layer-wise control method, lowering the laser power to compensate for the over-melt of the previous layer [24]. This method shows a dimensional accuracy improvement but cannot prevent the happening of heat accumulation in the first place since the compensation is applied to the following layer. Thus far, some efforts have been made on real-time laser power control. For example, Kruth et al. used both a high-speed CMOS camera and a photodiode to solve the over-melting issue on overhanging structures [8]. Their work demonstrated the concept, but the improvement is limited. The main problem is the low response time of the controller and the lack of signal pre-processing. Even though their sensing equipment has over 1 kHz capability, the sensor, computer, and controller communication create significant lag, limiting the effectiveness of the control. Such lag makes the system not close enough to the goal of real-time control.

Renken et al. recently implemented a PID-based control system by combining a pyrometer with a fast field programmable gate array (FPGA) [25]. The team claimed that the system's response time could be theoretically as low as $46 \mu\text{s}$. Still, they did not successfully yield any convincing experimental results to verify the system's effectiveness because trials were poorly designed and lacked measurement of printing accuracy and stabilizing time. Another issue with this work is that the system never converged to the target due to using only the proportional controller. Additionally, this work uses the standard deviation of the sensor signal as the control goal, which does not directly correlate to the printing shape accuracy. Shkoruta et al. used an image-based control method to regulate the laser power in L-PBF [26]. This work claimed they successfully stabilized the sensing signal but did not provide any measurement or image of the actual printed part. The effectiveness of their control remains unknown. Moreover, similar to Renken's work, Shkoruta et al. only used the proportional controller, which is insufficient for stabilizing the process. Therefore, no previous work has demonstrated effective real-time laser power control in L-PBF.

1.3. Research gap analysis and research outlines

When L-PBF uses constant process parameters to print, heat accumulation, humping, and denting could happen. These adverse effects will result in defects such as poor shape accuracy and surface quality. Among all the control methods, in-situ adaptive laser power control is hypothesized to achieve consistent melting in L-PBF effectively and thus investigated in this study. However, challenges remain in no available L-

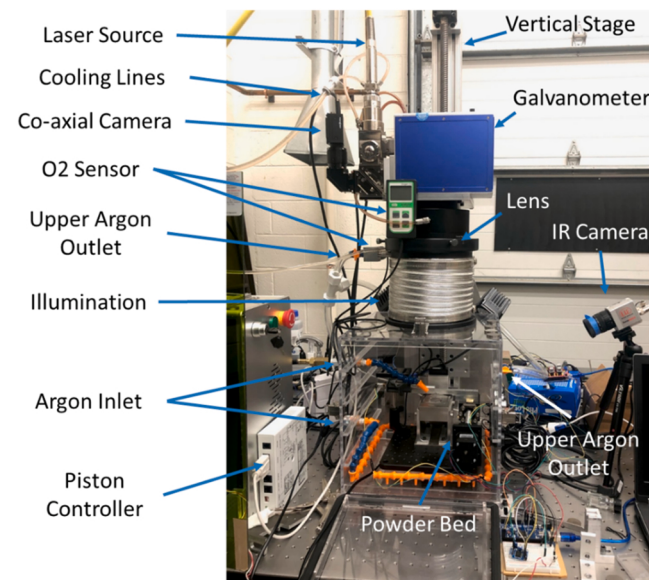


Fig. 2. The equipment layout of the customized L-PBF platform.

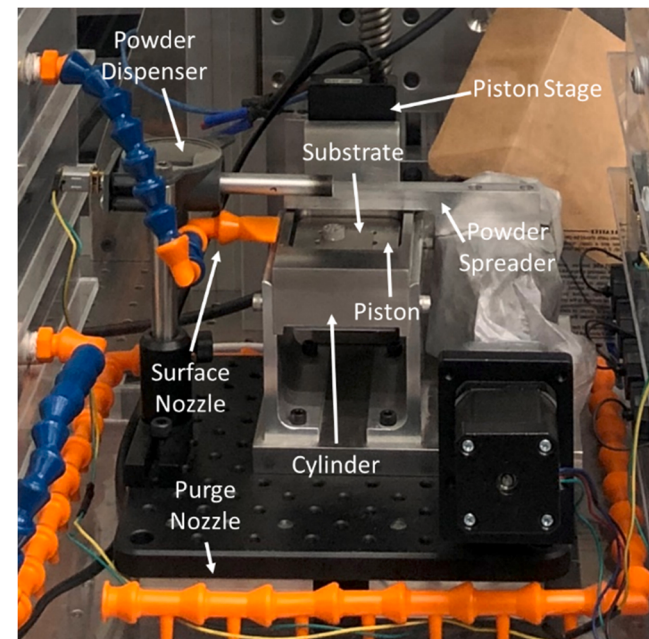


Fig. 3. The equipment layout of the powder bed.

PBF machine for adaptive laser power control, long signal processing time, high device communication lag, and lack of signal-to-quality correlations to determine the control setpoint.

To tackle the challenges identified above, a customized self-control L-PBF platform is implemented and presented in Section 2. Section 3 discusses the sensor's design, verification, calibration, and the necessary procedures for the closed-loop control of the laser power. In Section 4, the developed sensor and adaptive laser power control method are tested on a sample printing shape that contains regular and small features. Finally, Section 5 provides concluding remarks.

2. Implementation of the customized L-PBF platform

Since commercial machines are generally incapable of providing real-time monitoring data and being protected from in-process

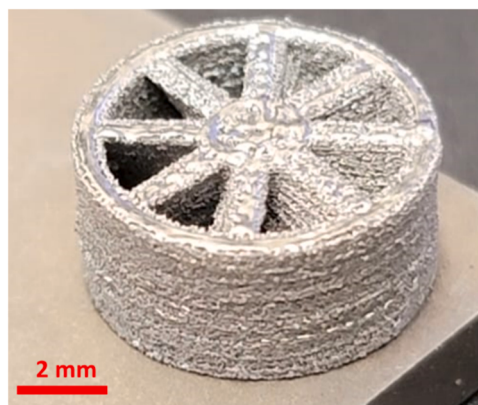


Fig. 4. A Ti-64 turbine nozzle print by the proposed L-PBF platform.

interventions, it is impossible to implement real-time feedback control. Therefore, this work first builds a customized L-PBF platform (Fig. 2). This platform solves the above issue using a modification-friendly design and equipping numerous sensors and sensor ports. The major components of this platform include a laser, optics, galvanometer, laser controller, chamber, cooling system, and powder bed system.

A Ytterbium continuous wave fiber laser beam (Raycus RFL-C1000, China) with 1000 W maximum power first enters a beam splitter which reflects the laser spectrum (1070 nm), then redirects by a galvanometer (PSI 20 M, China) to the printing surface. The galvanometer is mounted on a vertical stage to adjust the laser focus and the spot size. The laser head, galvanometer, and optics are cooled by a water chiller.

An adjustable aluminum pipe is installed between the chamber and the galvanometer, and the chamber is made out of static-free acrylic. Acrylic is chosen because it is transparent and ideal for process monitoring. The right-hand side of the chamber has multiple USB 3.0 and pin feedthroughs installed, enabling numerous sensors and actuators. The chamber is also equipped with two pairs of gas inlets and outlets, helping create a protective gas environment.

Inside the chamber is a powder bed fixture, as shown in Fig. 3. The powder bed consists of a powder dispenser, a powder spreader, and a piston-cylinder design powder bed. The piston is actuated by a high-precision (0.9 μm) linear stage (Newport MFA, USA). Currently, the printing area is restricted to a 25.4 by 25.3 mm^2 space for powder-saving purposes and can be easily upgraded to a larger size. The printing height is 25 mm, determined by the maximum travel distance of the piston stage. An Arduino-based controller drives the powder spreader and the dispenser, and the piston actuator is controlled by a programmable controller (Newport SMC 100PP, USA).

The platform has a customized high-speed IR camera (Micro-epsilon M1, Germany). The IR camera has a 50 mm zoom lens which yields an

$8 \times 11 \text{ mm}^2$ FOV. It runs at 1 kHz and has a 50 × 70 pixel resolution. A notch filter that blocks the laser spectrum is installed on the lens to protect the IR sensor, and the lens's aperture is set to f/20. Since the L-PBF process generally requires a protective gas environment, Argon, a very stable noble gas, is used in this platform. An oxygen meter (Apogee MO-200, USA) that measures as low as 0.1% concentration is used to monitor the printing environment.

Once the platform is filled with Argon, the powder dispenser will deposit a gentle amount of powder, and the spreader will apply it uniformly onto the substrate. The powder amount, spreader speed, and layer heights are adjustable through the easy-programmable controller. Fig. 4 shows an example Ti-64 turbine nozzle printed by this platform. This part's side wall quality $\text{Ra} = 5 \mu\text{m}$, measured by Surfometer, Precision Devices Inc., USA) is compatible with commercialized machines. However, the top surface quality, especially the spokes, suffers from humping and denting due to using constant laser power on short raster lines.

3. Controller and data acquisition system design

The control system utilizes the PID controller, a classic closed-loop control method that adjusts the process parameter according to a sensor's feedback (see Fig. 5) [27]. In a PID control loop, sensors periodically send the measurement back to the controller. Such measurement is compared with the setpoint target to estimate the error value $e(t)$. The error is then processed by proportional (P), integral (I), and derivative (D) calculations to generate the control strategy and adjust the process parameters. Individual gains, namely, K_p , K_i , and K_d , can scale the result of the P, I, and D terms by tuning. In this work, the control output is an analog 1–5 V signal, linearly representing 100–500 W laser power. The laser manufacturer has calibrated the linearity [28]. The measured voltage generated by the newly developed thermal sensor (discussed in Section 3.1.1) represents the thermal emission from the powder bed. It is named Thermal Emission Index (TEI) in this work. As discussed in the literature review, Wang et al. proved that thermal emission has a linear correlation with the melt pool size [22]. In this work, the TEI is correlated with the dimensional error for a control setpoint determination (discussed in Section 3.1.2).

As mentioned in Sections 1.2 and 1.3, the challenge of high-speed and real-time control mainly comes from two aspects, namely, the speed and lag of the control system. Speed refers to the time taken for measurements and related control computations, and lag means the inter-device communication time. For example, a high-speed camera can achieve high time frequency but has to store the data in a buffer before it can be transferred to the computer. Such a device is fast but has a long lag. The fast speed in this work is achieved by two approaches. First, instead of a sophisticated IR camera, an analog sensor (in this work, a light-dependent resistor, LDR) is used, which does not have intrinsic sensing frequency limitations. Second, the control decision is made using computationally effective algorithms. The low lag is

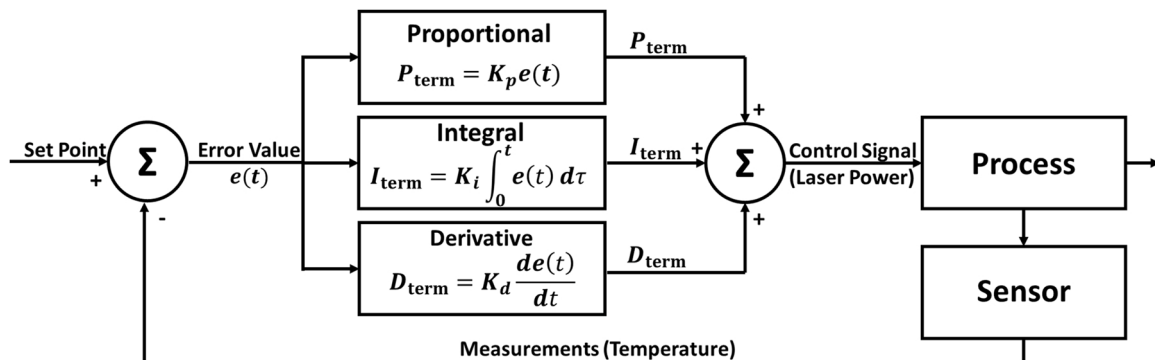


Fig. 5. Illustration of PID control [29].

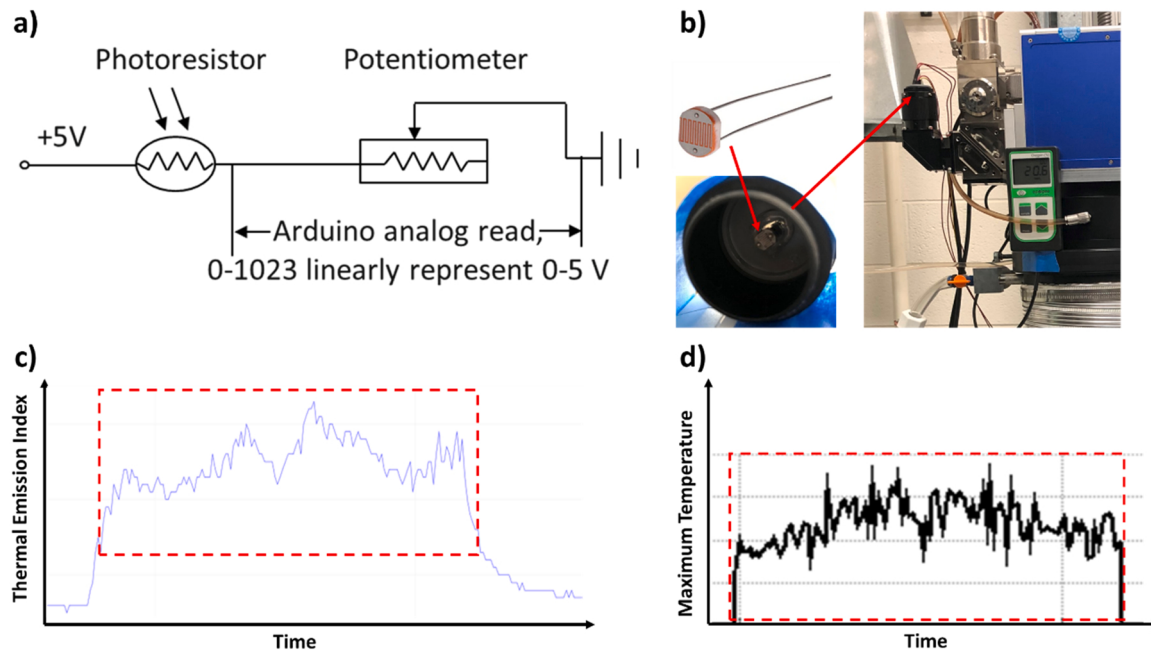


Fig. 6. a) The electrical diagram of the proposed sensor. b) The mounting illustration of the LDR. c) A sample monitoring result from the proposed sensor. d) The monitoring result (maximum temperature) of the same experiment from a high-end IR camera. The red dash region represents the same time span.

accomplished by completing the entire control loop without serial port communication. Specifically, the sensing and control programs are run on a dedicated Arduino, independent of a computer, significantly reducing the time needed for inter-devices communication (sensor-computer and computer-controller) and eliminating the need for a buffer. The sensor design and tuning method are elaborated in Section 3.1. The control and data acquisition programs are presented in Section 3.2.

3.1. Sensing system

3.1.1. Sensor design

This work uses an LDR (photoresistor)-based sensor to detect the powder bed thermal emission due to heating. The LDR is a resistor that changes its resistance depending on the number of photons it receives. The analog LDR used in this work has $2\text{ M}\Omega$ dark resistance and $20\text{ k}\Omega$ light resistance at 10 Lux. It has the advantage of no sensing frequency constraint (analog signals) and low cost. However, used as a high-speed thermal sensor, LDR has two disadvantages, namely, long responding time (30 ms to rise or dim fully) and insensitivity to the infrared spectrum. Nevertheless, they do not adversely influence the application in L-PBF. Specifically, for L-PBF power control, heavy data smoothing is needed since the laser switch on and off frequently during the printing, and sparks appear randomly. The responding time of the LDR can serve as a moving-average type of data smoother. The insensitive spectrum issue does not significantly influence the measuring capability of the LDR since the melting temperature of most metal materials used for 3D printing already generates a significant amount of visible light.

As Fig. 6a illustrates, the LDR is serially connected with a potentiometer (0.001 – 1 $\text{M}\Omega$) and powered by a 5 V power supply from the Arduino (model: Mega 2560, processor: ATmega2560, clock speed: 16 MHz, analog read time: 0.1 ms). The Arduino then uses its analog-read pin to read the potentiometer's voltage. Since the LDR's resistance drops with increasing light intensity, the voltage on the potentiometer will grow when the melt pool and surrounding temperature rise. This phenomenon makes the response analogous to a pyrometer. As Fig. 6b shows, the LDR is enclosed in a C-mount extension tube and mounted to the co-axial viewport of the platform. This setup helps eliminate the influence of laser location change and ambient light

fluctuation. The IR camera described in Section 2 is used to validate the result of the proposed sensor by monitoring the 3D printing simultaneously with the proposed sensor (synchronized by a software trigger). The reading from the proposed sensor (see Fig. 6c) and the maximum temperature reading of the IR camera (see Fig. 6d) share a very similar pattern, making it suitable for control. Notice that the proposed sensor has a broader sensitive range (the region outside of the red dash) than the high-temperature IR camera, which cannot sense thermal emission below 920 °C. These two figures do not show the temperature scale because they represent different meanings. The IR camera is only used for verifying if the developed LDR sensor is suitable for thermal-based PID control. During the high-speed real-time control, the IR camera is not used due to long communication lag with the computer. All the thermal data after Fig. 6d are collected from the LDR sensor.

3.1.2. Sensor tuning

Instead of a constant resistor, a potentiometer is used because it can adjust the sensitive range of the sensor. Even though the analog signal generated by the LDR has infinite resolution, an Arduino board's analog read can only provide $2^{10} = 1024$ different readings since it runs on a 10 Bit format. Specifically, the analog read function generates integers from 0 to 1023, representing 0 – 5 V voltage linearly and giving the setup a finite resolution. To achieve smooth control, the sensor's response at the temperature of interest needs to cover as many integers as possible.

For example, when the potentiometer's resistance is significantly higher than the LDR's resistance, the sensor's response is 1023 (represents 5 V). However, in this scenario, the change in LDR's resistance due to different printing temperatures cannot influence the voltage on the potentiometer, making the reading hard to distinguish between different printing conditions. On the other hand, when the potentiometer has a very small resistance compared with the LDR, no matter how the thermal emission changes, the LDR will take most of the voltages and make the sensor's reading close to zero, still unable to distinguish different printing conditions. Therefore, the resistance of the potentiometer needs to be tuned appropriately depending on the temperature range.

To optimize the sensor setting, we define a term called resolution of interest (ROI), which means the number of distinguishable values between the minimum and maximum printing temperature. By experiments, a heat accumulation will likely occur when raster lines are

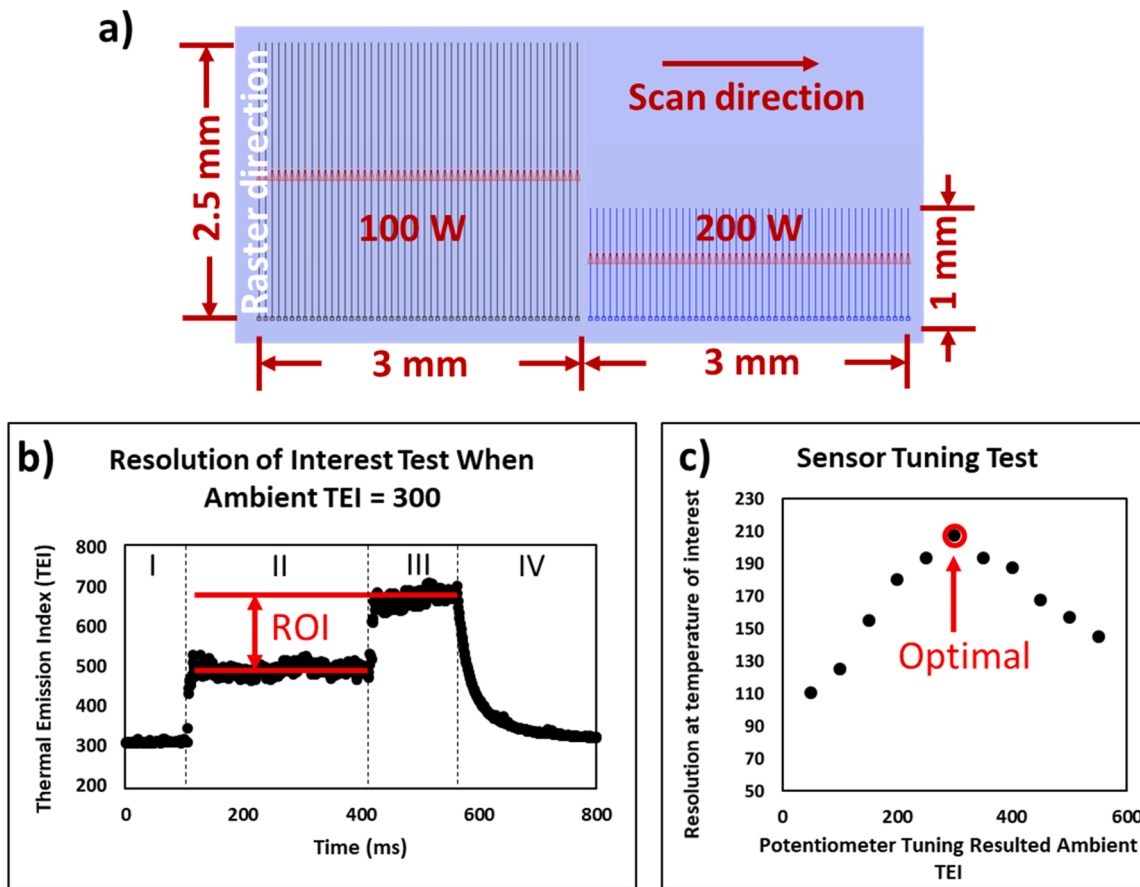


Fig. 7. a) The testing shape design (printing condition is Ti-64, 100 µm thickness, 55 µm hatch spacing, one-directional raster fill, 800 mm/s scan speed, 350 µs laser on/off delay), the first rectangle represents insufficient melt case and the second represents over melt scenario. b) A sample TEI pattern of the testing shape observed by the proposed sensor, where Region I, II, III, and IV represent ambient, insufficient melt, over melt, and cooling, respectively. c) The influence of sensor setting on the resolution of interest.

shorter than 2 mm. The minimum printing temperature is defined as when minimum laser power (100 W) is used to print a non-heat accumulation pattern (a rectangular shape filled with 2.5 mm raster lines). On the other hand, the maximum printing temperature is set as the temperature when heat accumulation occurs intensively (printing a miniature feature with a 200 W laser).

Tuning can be achieved by adjusting the potentiometer. The ambient light condition can be used to determine the sensor setting. A test pattern shown in Fig. 7a is designed to perform the tuning, consisting of both minimum and maximum printing temperature conditions. Fig. 7b shows an example of a TEI history pattern where both minimum and maximum printing temperature printing conditions can be observed clearly. In this figure, region I represents the ambient TEI reading. Region II and III represent the TEI of the first shape (2.5 mm raster and 100 W) and the second shape (1 mm raster and 200 W), respectively. Region IV represents the cooling to the ambient condition. This printing pattern has been repeated with different sensor setups (adjust the potentiometer to achieve, which will change the ambient TEI reading). The influence on ROI from the potentiometer is shown in Fig. 7c. The setting with 300 ambient TEI units is optimal and has 210 ROI. The ambient light condition will slightly change the sensor response. Therefore, the sensor tuning in this section and the control set point in Section 4.1 is only valid when the ambient light condition remains unchanged. This condition can be achieved by fixing the L-PBF machine location, blocking the room window, and keeping the same amount of ceiling lights on.

The sensor's noise level was tested by different constant light exposure levels (achieved by adjusting the aperture of the co-axial viewport that the sensor mounted on). The sensor's response all has a + / - 1 TEI

unit fluctuation. Therefore, the range of the signal-to-noise ratio depends on the sensor response range during the printing. This work defines the temperature of interest as the range between insufficient melt and over melt, corresponding to 490–700 TEI units with the 300 ambient TEI units setup. Therefore, the resulting signal-to-noise ratio ranges from 490 to 700.

3.2. Control and data acquisition programs

The sensor mentioned in Section 3.1 is connected with two Arduino boards in parallel, one for PID control and another for data acquisition. Three programs are developed to control, monitor, and archive the printing results. Specifically, the sensing and control program running on the first Arduino is named the *PID Arduino*. For real-time control purposes, this Arduino does not communicate with the computer. It captures the LDR signal and then calculates the PID result, which is sent as an analog signal to the laser generator. However, the laser power and thermal emission data must be logged for PID tuning, which requires communication with the computer. Therefore, a second Arduino was used dedicatedly for data logging so the communication does not influence the speed of the PID control that runs on the first Arduino. The monitoring program running on the second Arduino has been named the *Tunnel Arduino*. The data storing program running on a computer is responsible for logging values from *Tunnel Arduino* and initiating experiments, and it is called *Data Collector*. These three programs are presented in Sections 3.2.1, 3.2.2, and 3.2.3, respectively.

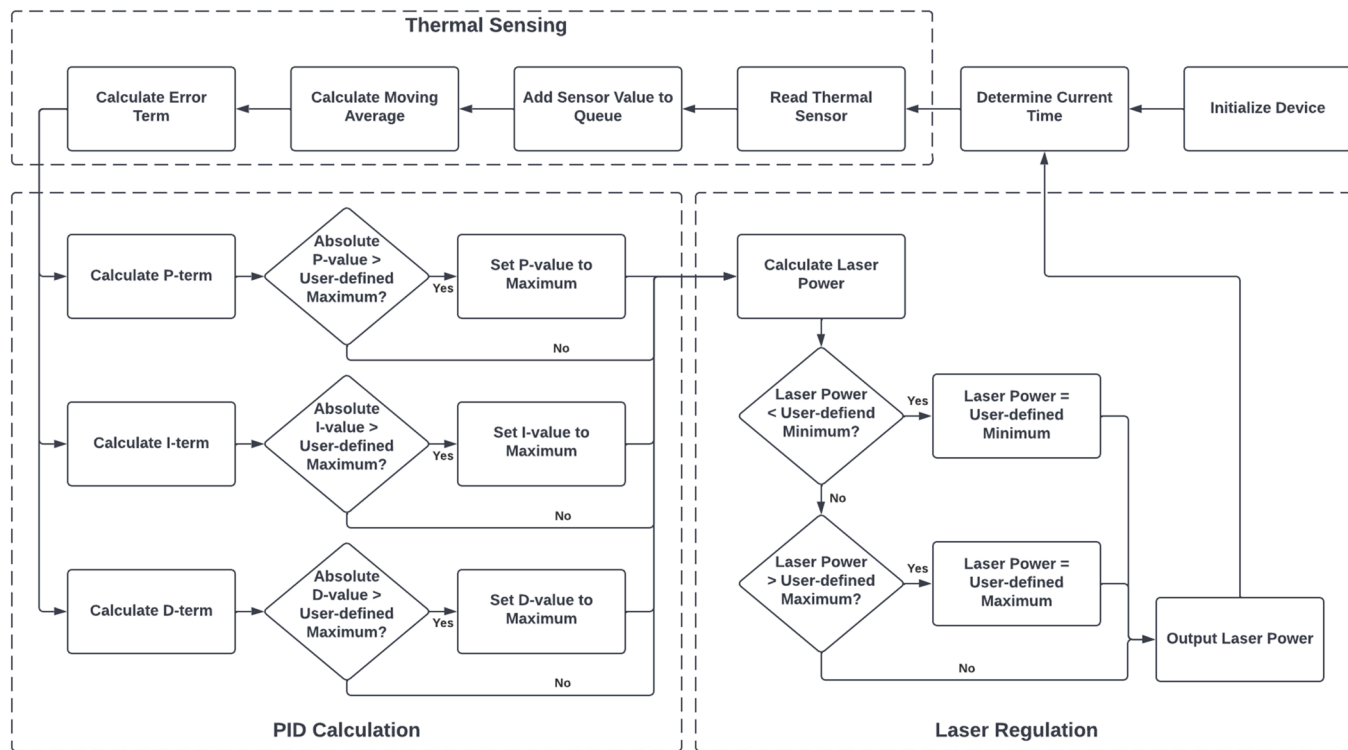


Fig. 8. Overview of PID Arduino Algorithm.

3.2.1. PID arduino program

The objective of the *PID Arduino* program is to adjust the laser power based on the thermal sensor developed in [Section 3.1](#). An overview of this algorithm is shown in [Fig. 8](#). It consists of three parts, namely, thermal sensing, PID calculation, and laser regulation. After the device (PID control Arduino) has been initialized, the time is recorded, then the thermal sensing module begins. The sensor connected to the PID control Arduino records the signal at 2 kHz. The raw value of this sensor's reading is stored in a queue of size ten and used to calculate the moving average. The moving average is then used as the measurement feedback

to the PID calculation module.

The moving average was used because the sensor data capturing and PID calculation do not stop when the laser turns off between two adjacent but disconnected melt tracks. This phenomenon will cause a dropping TEI and then mislead the PID calculation, making it try to increase the laser power incorrectly. To solve this issue, a moving average was applied since it can smooth the signal, removing the unwanted TEI drop. The moving average window size is a tradeoff between the controller settling time and the steady state control oscillation. This work determines the moving average window size by experimental

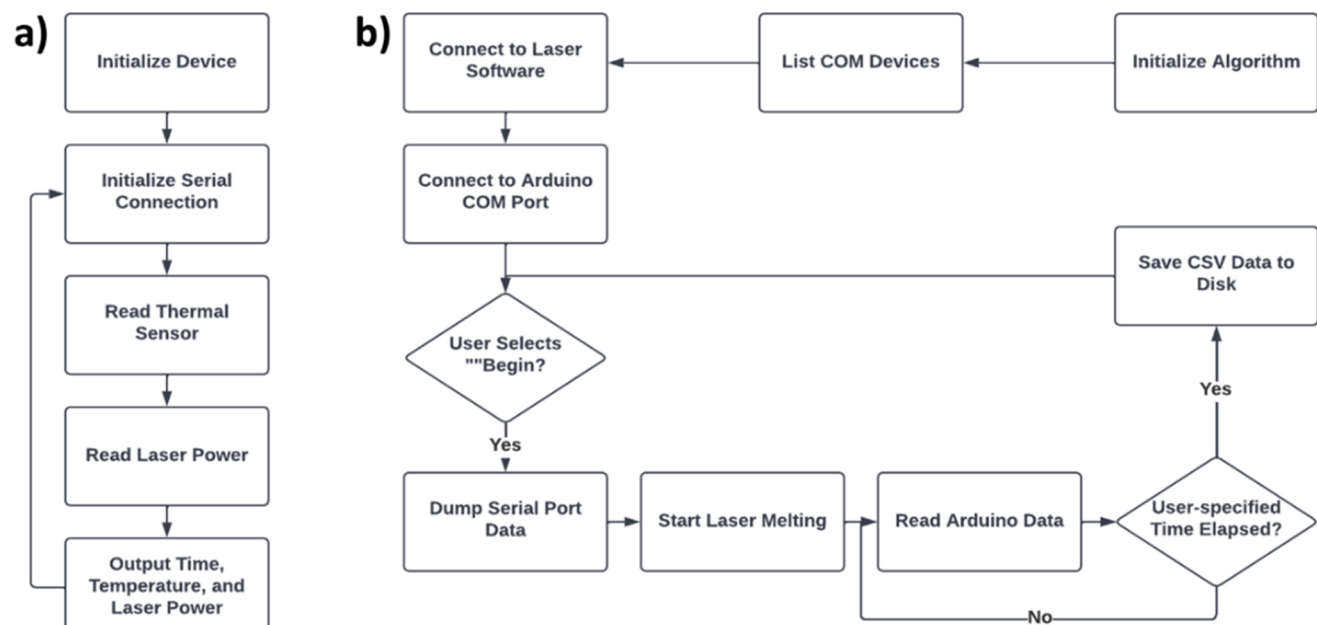


Fig. 9. a) Overview of Arduino Tunnel Algorithm. b) Overview of Data Collector Algorithm.

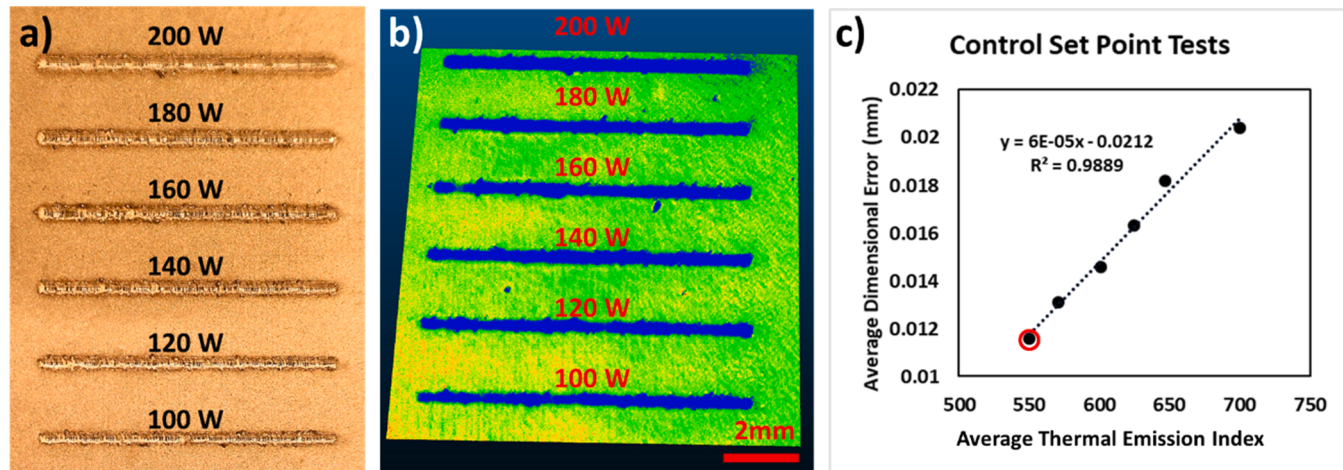


Fig. 10. a) Microscopic image of thin line printings. b) High spatial resolution 3D scanned data of thin line printings. c) Correlation between the average dimensional error and average thermal emission index of each thin line printing.

testing. An ideal window size is when the TEI fluctuation due to laser idle is less than 5.5 TEI units (1% of the target TEI). The resulting moving average window size is ten.

Since the system sense temperature at discrete time steps, the integrals and derivatives are calculated numerically. For example, to calculate the integral, the error is first calculated by comparing the sensing TEI with the Target TEI, then the result is multiplied by the frame time (0.5 ms for 2 KHz control). After that, the product is added to a variable which will eventually be multiplied by the integral coefficient K_i . This variable will be kept and updated for each control loop. As for the derivative calculation, the previous error will be extracted and used to compare with the current error to calculate the error difference. This difference will be then divided by the 0.5 ms time laps to complete the derivative calculation. After the current PID loop is completed, the current error will be stored as the previous error and used in the next control loop.

In this module, each P, I, and D calculation has a limiter function to prevent extreme adjustments. The calculation results are then passed to the laser regulation module. As a safety feature, the output laser power is also equipped with a limiter function that prevents extreme laser power during the PID tuning process. The laser power limiter function can also restrict the laser power from going below 100 W, the minimum laser output defined by the manufacturer. The digital laser power output will be sent to the laser generator as an analog signal by a digital-to-analog converter (model: PCF8591, tested output speed with Arduino Mega 2560: 3 kHz) driven by the Arduino.

3.2.2. Tunnel arduino program

The objective of the *Tunnel Arduino* program is to monitor the process without intrusion. An overview of the *Tunnel algorithm* is shown in Fig. 9a. This algorithm runs on the data acquisition Arduino. After the initialization, it reads the thermal sensor signal and laser power and outputs them with time stamps via a serial port to the computer.

3.2.3. Data collector program

The *Data Collector Program* has two tasks. First, it reads the sensor values from the *Tunnel Arduino* and stores them in a CSV file. Second, it triggers the laser. An overview of the *Data Collector* algorithm is shown in Fig. 9b. This program is written in C# language. A graphic user interface (GUI) is developed to let the user specify the COM port number, baud rate, and sensing duration. The baud rate is set to 500,000 in this work to balance the program's speed and stability. After launching the GUI, the program automatically tries to connect to the laser marking software through a TCP web socket. The Arduino can be connected by clicking the "Connect to Arduino" button based on the user selections.

The "Begin" button can initiate the data collection and experiment. The serial port's internal buffer is emptied upon beginning an experiment, and data is collected and stored over the user-defined recording time.

4. Results and discussion

This section is to test the performance and effectiveness of the controller. As mentioned in Section 1.2, the correlation between process signatures and final quality needs to be established first. The method is presented in Section 4.1. The control target has also been identified in this section. In Section 4.2, a shape with both regular and small features is designed to examine the controller. The result is then quantified by a high spatial resolution 3D scanner and point cloud comparison algorithms.

4.1. Control setpoint determination

Since this work uses the LDR-based sensor to guide the laser power control, the TEI is directly correlated with the average dimensional error, and the TEI corresponds to the smallest dimensional error will be the future control target. The target TEI is determined by a set of thin line experiments containing six 0.3 mm × 8 mm thin lines printed with different laser powers (100 W to 200 W with 20 W increases). For each experiment, the average dimensional error and average TEI are calculated. Thin line shapes were chosen because they are appropriate representations of small features and instantly accumulate heat. These lines are filled by one-directional raster lines with 55 μm hatch spacing. The powder and substrates are both made of Ti-64 (property provided in Appendix Table A1), and the powder size ranges from 15 to 53 μm (Carpenter Additive, USA). The laser spot size, speed, and layer height are 70 μm (1/e² diameter), 800 mm/s, and 30 μm, respectively. Additionally, a flat nozzle is used for blowing Argon gas at a 20 L/min flow rate above the printing surface to improve the printing quality.

The printed results are shown in Fig. 10a. A width increase can be observed from the lower power to the high power cases. This is due to the melt pool size increase. The thin lines are scanned by an in-house-built high-performance 3D scanner reported in Wang et al.'s work with 5 μm spatial resolution and 0.055 μm accuracy [30] (see Fig. 10b). The point cloud comparison method reported in that work was adopted to calculate the average dimensional error, which is the averaged point-to-mesh distance (C2M distance [30]) between the 3D-scanned point cloud data and the CAD model (0.3 mm (W) × 8 mm (L) × 0.03 mm (T)). The correlation between the average error and the average TEI is shown in Fig. 10c. This graph shows that the average geometry error linearly correlates with the TEI, and the error is minimal

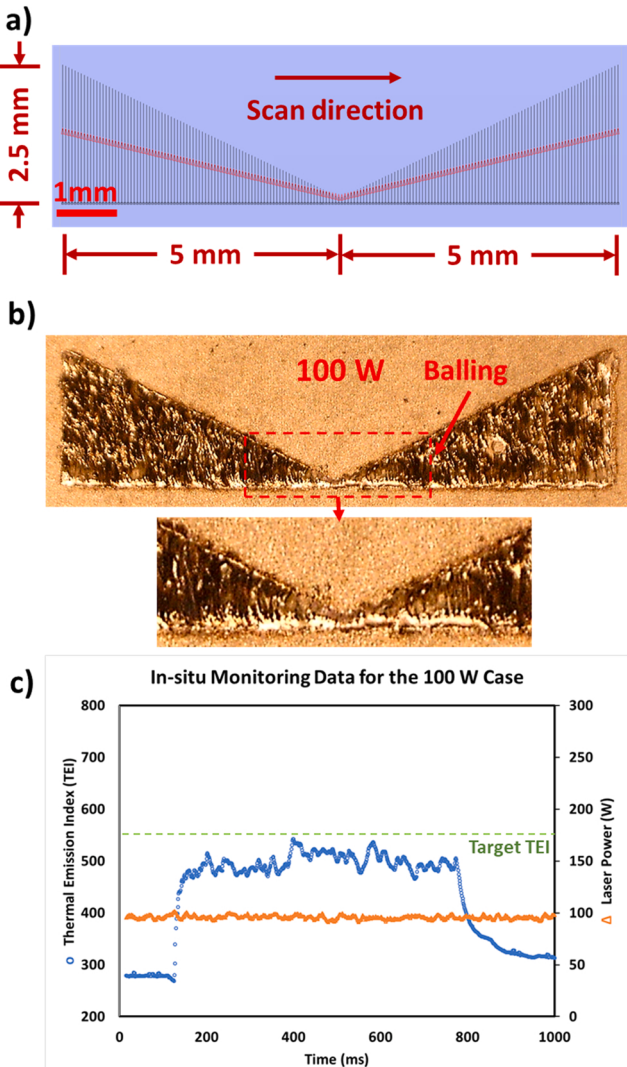


Fig. 11. a) The testing shape and laser scanning pattern illustration. b) The microscopic view of the printed result by 100 W constant laser power. c) The process monitoring data for the constant 100 W case.

when the sensor yield 550 TEI units, which will be used as the control target. This TEI refers to the 100 W power case, but directly printing a regular shape with such a low power is not feasible. More information is provided in Section 4.2. Notice that the designed geometry used for the point cloud comparison has a height of 30 μm . However, to compensate for the loose powder packing, 100 μm powder was applied.

4.2. Control experiment design and result analysis

To test the controller, a twin-triangle shape pattern is designed (See Fig. 11a). The beginning and end of the scan are not expected to have severe heat accumulation issues since the raster path is relatively long. In contrast, the central region has short raster lines and is expected to have severe heat accumulation and a larger melt pool. The shape is printed three times with 100 W constant laser power, 200 W constant laser power, and 100–200 W adaptive laser power, respectively. All other process conditions are the same as the experiments performed in Section 4.1. In the rest of this paper, these three cases are called constant 100 W case, constant 200 W case, and adaptive power case, respectively. The control target is set to 550 TEI units for the adaptive power case as Section 4.1 determined.

Fig. 11b shows a massive insufficient melt in the constant 100 W

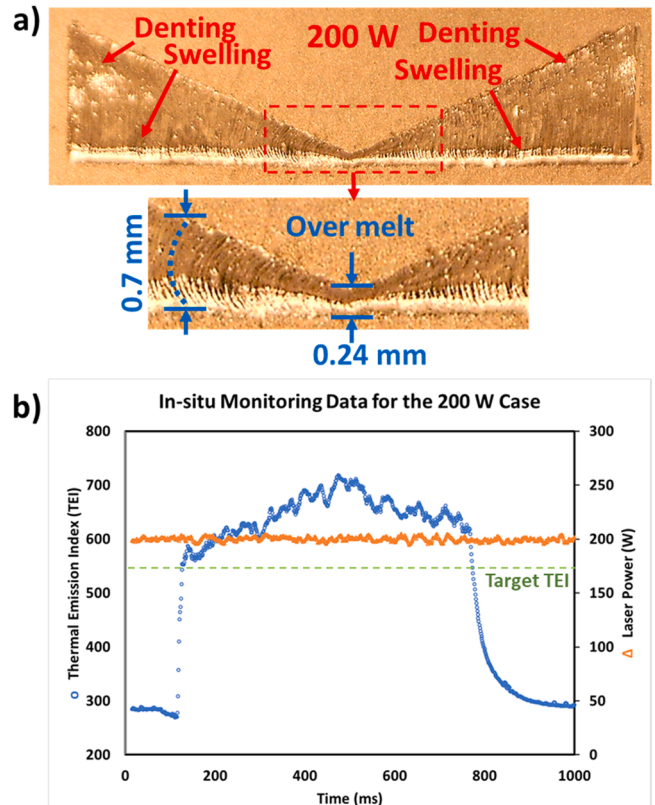


Fig. 12. a) The microscopic view of the printed result by 200 W constant laser power. b) The process monitoring data for the constant 200 W case.

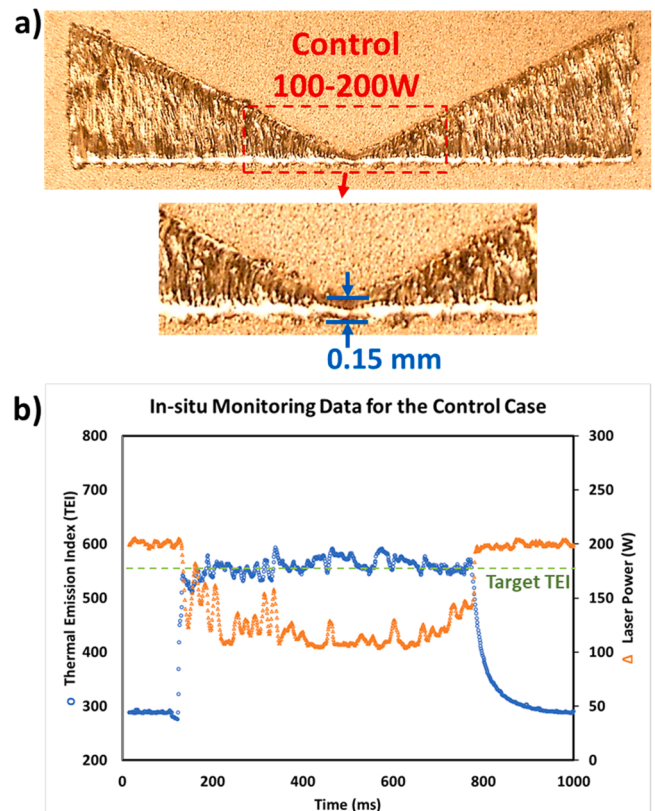


Fig. 13. a) The microscopic view of the printed result by 100–200 W adaptive laser power. b) The process monitoring data for the adaptive power case.

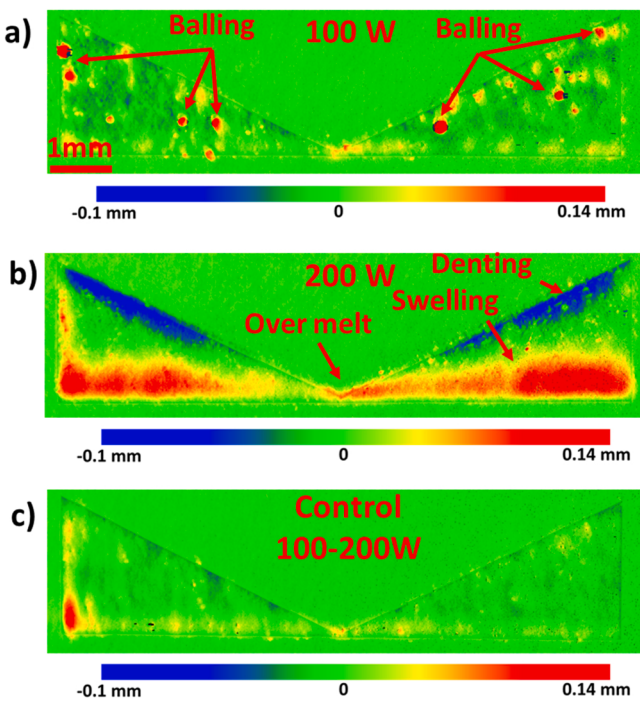


Fig. 14. a) The 3D scanning result of the constant 100 W case. b) The 3D scanning result of the constant 200 W case. c) The 3D scanning result of the adaptive power case.

case. It is represented by balling, high surface roughness, and black burn marks. No over-melt issue was observed, confirmed by the low TEI shown in Fig. 11c. Specifically, the TEI stays at around 500 TEI units, and only minor heat accumulation occurs. However, such a severe insufficient melt is unacceptable in L-PBF because fully-dense parts cannot be created, and powder spreaders will be severely damaged by the balling.

As for the constant 200 W case, the insufficient melt is replaced by denting and humping (see Fig. 12a). Severe over-melt can be observed in this case. The zoom-in view of Fig. 12a shows an oversized melting region in the center area, causing shape inaccuracy. The narrow triangle tip has a width of 0.24 mm, which ideally should be zero. Curved wrinkles (one example marked in blue dash) indicate that the vast melt pool can span over 0.7 mm, creating a different cooling rate and thermal gradient compared with other areas. The change in the solidification will result in microstructure inconsistency. The thermal history data indicates the temperature of the melt pool grows while the raster line shortens. The TEI starts from around 580 TEI units and peaks at around 720 TEI units due to heat accumulation. Unlike the symmetrical printing pattern, the thermal emission monitoring data in Fig. 12b is

asymmetrical. The second (right-hand side) triangle has a higher TEI than the first. This phenomenon is due to the heat accumulation from the first triangle, making the TEI around 610 TEI units when the laser shuts off, higher than at the beginning (580 TEI units).

As for the adaptive power case, insufficient melt, balling, over melt, and humping/denting, were not observed from the microscopic inspection (see Fig. 13a). The central region has a very sharp triangle tip and is free of curved wrinkles compared with the constant 200 W case. The triangle tip has a width of 0.15 mm, significantly smaller than the constant 200 W case (0.24 mm). The process monitoring data shows the thermal emission has been successfully stabilized to 550. The laser power responds consistently according to the sensor data (see Fig. 13b). The laser power is reduced from 200 W to 110 W when the raster line shortens and increases to 150 W towards the end of the scan. Since the L-PBF process is highly dynamic, the heuristic tuning method is used instead of rule- or model-based tuning to determine the PID's gain terms [27]. The process monitoring data is recorded and examined when a new gain combination is tested (tunable gains are explained in Fig. 8). The heuristic tuning strategy is as follows: increase K_p until oscillation occurs, then gently increase K_d to remove the oscillation; repeat the first step until changing the K_d cannot further stabilize the process, then use the latest stable setting as the final. This work did not use the integral term (K_i) since the utilization of P and D gains has yielded satisfactory results. The K_d and K_d used is 0.0006 and 0.03, respectively.

The 3D scanning and point cloud comparison method adapt in Section 4.1 is also used in this section. The errors are visualized in Fig. 14. The blue color represents a negative error (dent or lack of material added to the substrate), and red means a positive error (swelling or balling). For the constant 100 W case, numerous balling regions can be observed (Fig. 14a). The left-hand side triangle, especially the first half, has more blue regions than the right-hand side triangle, meaning the left-hand side triangle has a more severe insufficient melt than the right-hand side one. This result is because the printing direction is from left to right. Therefore, the later printed region has a slightly higher temperature due to heat accumulation, making the insufficient melt less severe (Fig. 11c verifies this). Denting and swelling are observed for the 200 W case (Fig. 14b). The red color in the center triangle tip region indicates this case suffers from over melt and shape inaccuracy. In contrast, the error map for the adaptive power case has the largest green areas, which suggests it has the least dimensional error (see Fig. 14c). Notice that the left bottom corner has a little hump. This phenomenon is because the controller needs time to respond. The monitoring data in Fig. 13b indicates that the stabilization time is around 8 ms, roughly representing the time required for two raster laser scan paths.

Fig. 15 provides the error histograms for all three cases. The error statistics, such as average, maximum, and standard deviation, are also provided in each histogram. By comparing Fig. 15a, b, and c, the one for the constant 200 W case, spreads the most (see Fig. 15b), indicating significant errors. In contrast, the error histogram for the adaptive

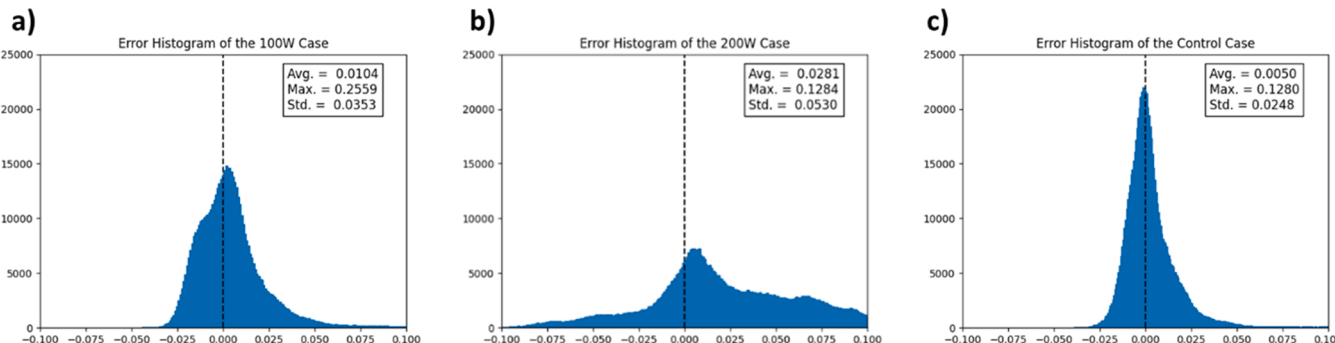


Fig. 15. a) The geometric error histogram of the constant 100 W case. b) The geometric error histogram of the constant 200 W case. c) The geometric error histogram of the adaptive power case.

Table A1

L-PBF Ti-64 properties [22,31].

Direction	Yield Strength (MPa)	Tensile Strength (MPa)	Tensile Strain %	Young's Modulus (GPa)	Liquidus Temperature (°C)	Solidus Temperature (°C)	Maximum Melt Pool Temperature (°C)
longitudinal	964	1041	7	113	1655	1604	3561
transversal	1058	1114	3	109			

power case is very center-concentrated, indicating most of the error is close to zero (see Fig. 15c). The average error for the adaptive power case is only 0.005 mm, significantly less than those of the constant 200 W case (0.0281 mm) and the constant 100 W case (0.0104 mm). As for the maximum error, the constant 100 W case has the highest 0.256 mm (Fig. 15a). This result is mainly due to the balling effect. As Fig. 14a illustrates, all the deep red (large positive error) regions have circular shapes representing balling. The adaptive power case did not significantly outperform the constant 200 W case in the maximum error (0.1280 mm compared with 0.1284 mm). This is due to the right bottom humping in the adaptive power case, which does not reflect the overall quality. The standard deviation of the adaptive laser power case (0.0248 mm) is significantly better than the other two (constant 100 W case: 0.0353 mm, constant 200 W case: 0.0530 mm), indicating a very uniform print. The constant 200 W case has the worst error standard deviation, mainly caused by swelling and denting since these issues are general and influence most of the printing area.

5. Conclusions

This work aims to solve the printing quality issues in L-PBF caused by constant printing parameters through high-speed real-time adaptive laser power control. An LDR-based low-cost and high-speed control system is designed and fabricated. The method to tune the sensor, the procedure to determine the control setpoint, and the programs to enable the control process have been developed. A customized smart L-PBF testbed was established to implement the feedback controller. It can produce not only high-quality parts but is also available for in-situ sensing and control. Verified by a set of actual Ti-64 printing tests, the controller successfully stabilized the melt pool size by regulating the laser power at 2 kHz. Microscopic imaging and high spatial resolution 3D scanning were used to validate the result. The analysis shows that the average and the standard deviation of the dimensional error of the case using the controller significantly outperform the constant laser power cases. The proposed controller costs less than \$50 and can work independently without a computer. It has excellent potential to be implemented on all L-PBF machines for product quality assurance.

CRediT authorship contribution statement

Rongxuan Wang: Writing – review & editing, Writing – original draft, Visualization, Validation, Software, Methodology, Investigation, Formal analysis, Data curation, Conceptualization. **Benjamin Standfield:** Validation, Software, Investigation, Data curation. **Chaoran Dou:** Validation, Software, Investigation, Data curation. **Andrew Chung Chee Law:** Writing – review & editing, Investigation, Data curation. **Zhenyu James Kong:** Writing – review & editing, Supervision, Resources, Project administration, Methodology, Funding acquisition, Conceptualization.

Declaration of Competing Interest

The authors declare that they have no known competing financial interests or personal relationships that could have appeared to influence the work reported in this paper.

Data Availability

Data will be made available on request.

Acknowledgments

The research reported in this publication was supported by the Office of Naval Research under Award Number N00014-18-1-2794. The authors would like to thank Scott Lancaster, Randall Waldron, Kelly Snidow, Chris Collins, Joe Linkous, Travis Lyons, and Mark Montgomery from Virginia Tech for assisting with platform setup and substrate fabrication.

Appendix

See Appendix Table A1.

References

- [1] M. Bisht, et al., Correlation of selective laser melting-melt pool events with the tensile properties of Ti-6Al-4V ELI processed by laser powder bed fusion, *Addit. Manuf.* 22 (2018) 302–306.
- [2] Z. Gan, et al., Benchmark study of thermal behavior, surface topography, and dendrite microstructure in selective laser melting of Inconel 625, *Integr. Mater. Manuf. Innov.* 8 (2) (2019) 178–193.
- [3] B. Richter, et al., High-speed X-ray investigation of melt dynamics during continuous-wave laser remelting of selective laser melted Co-Cr alloy, *CIRP Ann.* 68 (1) (2019) 229–232.
- [4] L. Thijss, et al., Fine-structured aluminium products with controllable texture by selective laser melting of pre-alloyed AlSi10Mg powder, *Acta Mater.* 61 (5) (2013) 1809–1819.
- [5] I. Campbell, et al., Wohlers report 2018: 3D printing and additive manufacturing state of the industry: annual worldwide progress report, Wohlers Associates, 2018.
- [6] C. Zhao, et al., Real-time monitoring of laser powder bed fusion process using high-speed X-ray imaging and diffraction, *Sci. Rep.* 7 (1) (2017) 1–11.
- [7] S.V. Chernyshikhin, et al., The Study on Resolution Factors of LPBF Technology for Manufacturing Superalastic NiTi Endodontic Files, *Materials* 15 (19) (2022) 6556.
- [8] J.-P. Kruth, et al., Feedback control of selective laser melting. Proceedings of the 3rd international conference on advanced research in virtual and rapid prototyping, Taylor & Francis Ltd, 2007.
- [9] N. Boone, et al., Thermal near infrared monitoring system for electron beam melting with emissivity tracking, *Addit. Manuf.* 22 (2018) 601–605.
- [10] C. Tang, K. Le, C. Wong, Physics of humping formation in laser powder bed fusion, *Int. J. Heat. Mass Transf.* 149 (2020), 119172.
- [11] Q. Wang, et al., Model-based feedforward control of laser powder bed fusion additive manufacturing, *Addit. Manuf.* 31 (2020), 100985.
- [12] H. Yeung, et al., Implementation of advanced laser control strategies for powder bed fusion systems, *Procedia Manuf.* 26 (2018) 871–879.
- [13] H. Yeung, B. Lane, J. Fox, Part geometry and conduction-based laser power control for powder bed fusion additive manufacturing, *Addit. Manuf.* 30 (2019), 100844.
- [14] H. Yeung, et al., *Laser path planning and power control strategies for powder bed fusion systems*. in: 2016 International Solid Freeform Fabrication Symposium, University of Texas at Austin, 2016.
- [15] N. Raghavan, et al., Localized melt-scan strategy for site specific control of grain size and primary dendrite arm spacing in electron beam additive manufacturing, *Acta Mater.* 140 (2017) 375–387.
- [16] R.R. Dehoff, et al., Site specific control of crystallographic grain orientation through electron beam additive manufacturing, *Mater. Sci. Technol.* 31 (8) (2015) 931–938.
- [17] M. Shao, et al., The effect of beam scan strategies on microstructural variations in Ti-6Al-4V fabricated by electron beam powder bed fusion, *Mater. Des.* 196 (2020), 109165.
- [18] K.S. Ramani, et al., SmartScan: an intelligent scanning approach for uniform thermal distribution, reduced residual stresses and deformations in PBF additive manufacturing, *Addit. Manuf.* 52 (2022), 102643.
- [19] E. Malekipour, et al., *Optimization of Chessboard Scanning Strategy Using Genetic Algorithm in Multi-Laser Additive Manufacturing Process*. in: ASME International Mechanical Engineering Congress and Exposition, American Society of Mechanical Engineers, 2020.

- [20] S. Clijsters, et al., In situ quality control of the selective laser melting process using a high-speed, real-time melt pool monitoring system, *Int. J. Adv. Manuf. Technol.* 75 (5) (2014) 1089–1101.
- [21] Liu, C., et al. Real-time 3D surface measurement in additive manufacturing using deep learning. in Solid freeform fabrication 2019: proceedings of the 30th annual international, solid freeform fabrication symposium—an additive manufacturing conference. 2019.
- [22] R. Wang, et al., In situ melt pool measurements for laser powder bed fusion using multi sensing and correlation analysis, *Sci. Rep.* 12 (1) (2022) 1–17.
- [23] T. Kurzynowski, et al., Effect of scanning and support strategies on relative density of SLM-ed H13 steel in relation to specimen size, *Materials* 12 (2) (2019) 239.
- [24] E. Vasileska, et al., Layer-wise control of selective laser melting by means of inline melt pool area measurements, *J. Laser Appl.* 32 (2) (2020), 022057.
- [25] V. Renken, et al., In-process closed-loop control for stabilising the melt pool temperature in selective laser melting, *Prog. Addit. Manuf.* 4 (4) (2019) 411–421.
- [26] A. Shkoruta, S. Mishra, S.J. Rock, Real-time image-based feedback control of laser powder bed fusion, *ASME Lett. Dyn. Syst. Control* 2 (2) (2022).
- [27] M.A. Johnson, M.H. Moradi, *PID control*, Springer, 2005.
- [28] Laser, R., User Guide of 1000W Small Size Cutting Continuous Wave Laser. 2021.
- [29] H.O. Bansal, Tuning of PID controllers using simulink, *Int. J. Math. Model. Simul. Appl.* 2 (3) (2009) 337–344.
- [30] R. Wang, et al., Development of structured light 3D-scanner with high spatial resolution and its applications for additive manufacturing quality assurance, *Int. J. Adv. Manuf. Technol.* 117 (3) (2021) 845–862.
- [31] M. Shummugavel, A. Polishetty, G. Littlefair, Microstructure and mechanical properties of wrought and additive manufactured Ti-6Al-4 V cylindrical bars, *Proc. Technol.* 20 (2015) 231–236.